Title

Laser-heated capillary discharge plasma waveguides for electron acceleration to 8 GeV

Journal

Physics of Plasmas, 27(5)

ISSN

1070-664X

Authors

Gonsalves, AJ
Nakamura, K
Benedetti, C
et al.

Publication Date

2020-05-01

DOI

10.1063/5.0002769

Peer reviewed

Laser-heated capillary discharge plasma waveguides for electron acceleration to 8 GeV.*

A. J. Gonsalves,[1,†] K. Nakamura,[1] C. Benedetti,[1] C. V. Pieronek,[1,2] S. Steinke,[1] J. H. Bin,[1] S. S. Bulanov,[1] J. van Tilborg,[1] C. G. R. Geddes,[1] C. B. Schroeder,[1,2] J. Daniels,[1] Cs. Tóth,[1] L. Obst-Huebl,[1] R. G. W. van den Berg,[3] G. Bagdasarov,[4,5] N. Bobrova,[4] V. Gasilov,[4,5] G. Korn,[6] P. Sasorov,[4,6] W. P. Leemans,[1,2,‡] and E. Esarey[1]

[1] *Lawrence Berkeley National Laboratory, Berkeley, CA, 94720, USA*
[2] *University of California, Berkeley, CA, 94720, USA*
[3] *University of Eindhoven, 5612 AE Eindhoven, Netherlands*
[4] *Keldysh Institute of Applied Mathematics RAS, Moscow 125047, Russia*
[5] *National Research Nuclear University MEPhI (Moscow Engineering Physics Institute), Moscow 115409, Russia*
[6] *Institute of Physics ASCR, v.v.i. (FZU), ELI-Beamlines Project, 182 21 Prague, Czech Republic*

(Dated: April 17, 2020)

A plasma channel created by the combination of a capillary discharge and inverse Bremsstrahlung laser heating enabled the generation of electron bunches with energy up to 7.8 GeV in a laser-driven plasma accelerator. The capillary discharge created an initial plasma channel and was used to tune the plasma temperature, which optimized laser heating. Although optimized colder initial plasma temperatures reduced the ionization degree, subsequent ionization from the heater pulse created a fully ionized plasma on-axis. The heater pulse duration was chosen to be longer than the hydrodynamic timescale of ≈ 1 ns, such that later temporal slices were more efficiently guided by the channel created by the front of the pulse. Simulations are presented that show this thermal self-guiding of the heater pulse enabled channel formation over 20 cm. The post-heated channel had lower on-axis density and increased focusing strength compared to relying on the discharge alone, which allowed for guiding of relativistically intense laser pulses with peak power of 0.85 PW and wakefield acceleration over 15 diffraction lengths. Electrons were injected into the wake in multiple buckets and times, leading to several electron bunches with different peak energies. To create single electron bunches with low energy spread, experiments using localized ionization injection inside a capillary discharge waveguide were performed. A single injected bunch with energy 1.6 GeV, charge 38 pC, divergence 1 mrad, and relative energy spread below 2 percent full width half maximum was produced in a 3.3 cm-long capillary discharge waveguide. This development shows promise for mitigation of energy spread and future high-efficiency staged acceleration experiments.

PACS numbers: 52.38.Kd

I. INTRODUCTION

Due to their small size, laser plasma accelerators (LPAs) [1, 2] are being investigated for a variety of applications, including free-electron lasers [3–7], Thomson sources [8–12], and electron-positron colliders with TeV energy [13–15]. For future TeV accelerators using PW-class laser systems, single-stage energy gains near 10 GeV are required for maximum efficiency and collider compatible beams [14].

In order to achieve ≈10 GeV energy gain using a PW laser system, the plasma density must be set appropriately. This is due to the fact that the accelerating gradient scales as $E_z \propto n_0^{1/2}$, and the effective accelerator length is limited by either the dephasing length or the laser depletion length, both of which scale as $L \propto n_0^{-3/2}$ [1]. Typically for guided lasers at lower intensities, beam-wave dephasing dominates before significant laser depletion; however, for the high laser intensities considered in this work, depletion of the laser energy is the main effect limiting the acceleration length. From these scalings, the energy gain of a single-stage LPA scales inversely with plasma density, n_0. Recently, reducing the density relative to past experiments [16–19] to $n_0 \approx 2.7 \times 10^{17}$ cm^{-3} allowed for the generation of electron beams with energy up to 7.8 GeV [20], as shown in Figure 1. In addition to lowering the plasma density, diffraction of the focused laser pulses had to be mitigated in order to accelerate over the full laser-depletion length and achieve maximum energy gain. This laser pulse guiding was achieved with a preformed plasma channel, in which the electron density is lower on-axis, creating a refractive index profile that is peaked on-axis [21]. For a parabolic channel with density rise (channel depth) Δn at a radius r_{ch} given by $n(r) = n_0 + (\Delta n / r_{ch}^2) r^2$, a low intensity, transversely Gaussian laser pulse can propagate with constant spot size when the input laser mode size r_0 is equal to the matched spot size of the channel r_m, where r_0 is the radius at which the focused laser pulse intensity drops by $1/e^2$ of the peak value, and $r_m = [\pi r_e (\Delta n / r_{ch}^2)]^{-1/4}$, where r_e is the classical electron radius. Lower r_m corresponds to a plasma channel with stronger focusing force.

* Paper N13.00003 Idontknow. **??**, ???, 2019
† ajgonsalves@lbl.gov
‡ Now at Deutsches Elektronen-Synchrotron

The capillary discharge waveguide [22] has been used to create plasma channels and increase the maximum beam energy available from LPAs [19, 23, 24]. For these plasma channels, some independent control over $r_{\rm m}$ and n_0 is possible by adjusting the diameter of the capillary $D_{\rm cap}$ since $r_{\rm m} \propto n_0^{-1/4} D_{\rm cap}^{1/2}$ [25]. However, in practice the diameter of the capillary must be large enough to avoid laser damage, and for available petawatt pulses, it was previously not possible to simultaneously achieve the required matched spot size ($< 70\,\mu$m) and plasma density ($< 4 \times 10^{17}\,{\rm cm}^{-3}$) to generate high energy beams such as those in Figure 1 [20]. In order to meet these requirements the capillary discharge waveguide was enhanced with inverse Bremsstrahlung (IB) from an additional "heater" laser pulse.

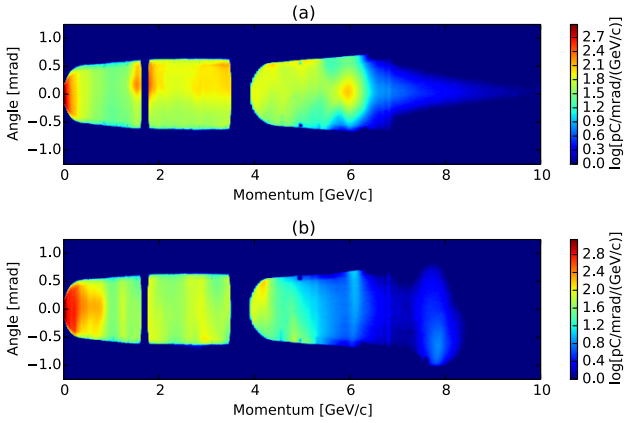

FIG. 1. Electron beams generated by propagating laser pulses with peak power 850 TW through a laser-heated capillary discharge waveguide. In (a) $n_0 = 3.4 \times 10^{17}$ cm^{-3} and $r_{\rm m} = 69\,\mu$m. In (b) $n_0 = 2.7 \times 10^{17}$ cm^{-3} and $r_{\rm m} = 61\,\mu$m. The total charge of the beams measured by the phosphor screen was 270 pC in (a) and 420 pC in (b).

In this paper we describe the physics of laser heating and channel formation with experiments and simulations, and the path to higher energy and higher quality electron beams with petawatt lasers. In the experiments of Ref. [20], guiding from the capillary discharge waveguide and self-guiding of the heater pulse were critical for channel formation over the full length of the accelerator. Here, we present an in-depth characterization and analysis of the relevant processes at play. Specifically, in Sec. II the role of heater pulse self-guiding is shown via magnetohydrodynamic (MHD) simulations. They show that even though there are strong head to tail changes in the propagation of the heater pulse, channels with percent-level longitudinal uniformity can be produced. Experimental evidence for heater self-guiding is presented in Sec. III A with heater pulse transmitted mode measurements and in Sec. III B with short probe pulse guiding. It was shown in Ref. [20] that the initial electron temperature T_e was an effective control over plasma heating and channel properties. Specifically, lower pre-heater temperature plasmas produced the low density channels with lower $r_{\rm m}$. However, one concern of reduced temperature is incomplete ionization, which could be detrimental to laser and heater guiding. In Sec. III C this is examined via ionization induced blueshifting of a probe pulse, as well as through MHD simulations. Additional experimental confirmation for the measured channel properties is provided in Sec. III D by comparing simulated and measured spectra of high power laser pulses transmitted through the capillary. And lastly, on the accelerator side, Sec. IV discusses the path to higher electron beam energy, while Sec. V shows initial experiments on improving the quality of multi-GeV electron beams with controlled injection techniques.

II. CHANNEL FORMATION PHYSICS

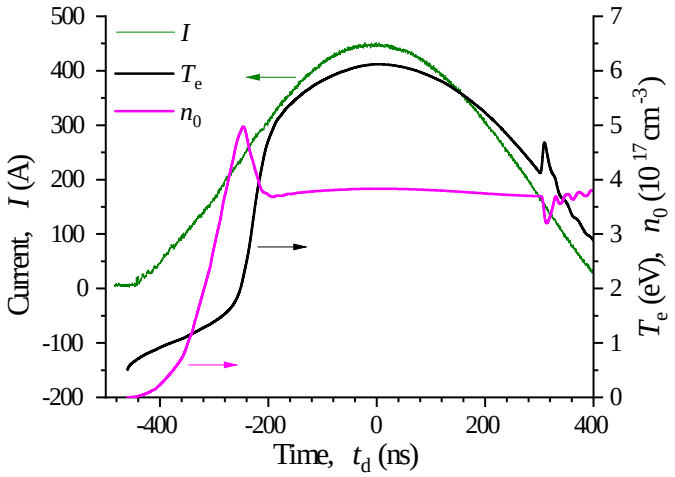

FIG. 2. The measured discharge current temporal profile (green), along with the simulated on-axis temperature (black), and density (magenta). The heater pulse arrived at time 300 ns, causing the short-duration temperature rise and density reduction. Figure taken from A. J. Gonsalves et al, Physical Review Letters 122, 084801 (2019) [20].

A laser-heated capillary discharge [20, 26] operates in the following way. An electrical discharge is struck in a capillary filled with hydrogen gas. The discharge creates a plasma that undergoes Ohmic heating, and a plasma with a density minimum on axis is formed due to cooling at the capillary wall. Subsequently, a laser pulse heats the plasma on-axis and deepens the plasma channel through hydrodynamic expansion, mitigated partially by thermal conduction [21]. For the density range relevant to this work, $n_0 = (2\text{–}5) \times 10^{17}$ cm^{-3}, theory and simulation of IB heating provide insight into the heating process and rates [27, 28]. The heating rate can be controlled by the laser intensity I, density n_i, heater laser wavelength λ_h and electron temperature T_e. The IB absorption is described by the imaginary part of the per-

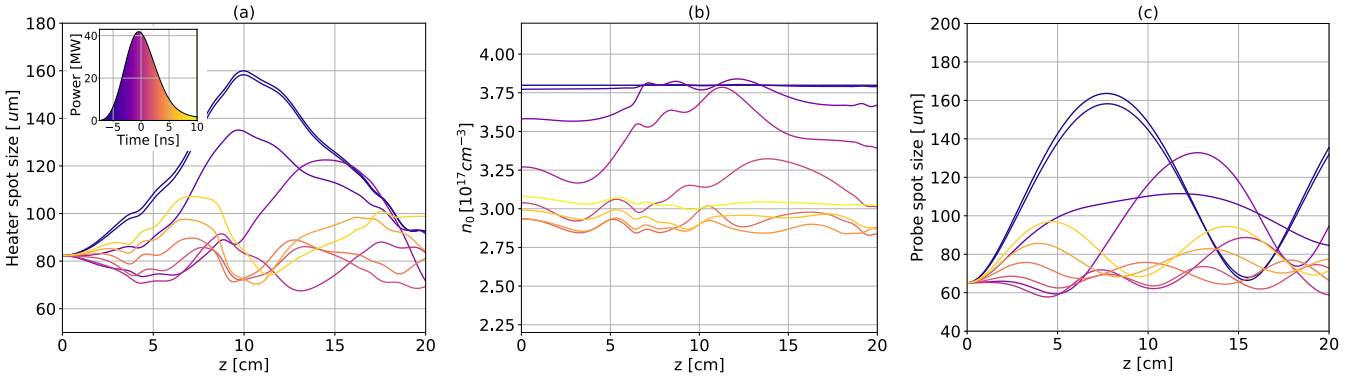

FIG. 3. Simulation of channel formation for heater pulse arrival 320 ns after the peak of the discharge pulse and initial hydrogen atomic density $6.12 \times 10^{17}\mathrm{cm}^{-3}$. Inset of (a): Temporal profile of the heater pulse with energy 0.3 J, with the color scale indicating the temporal slice for subsequent plots. The dark blue and orange colors correspond to the front and back slices of the heater pulse, respectively. (a-c) show laser and channel properties for different time slices 2 ns apart as a function of propagation distance z. The heater pulse near field (at the focusing lens) profile was taken to be top hat. (a) Spot size of the heater pulse. While the front of the pulse oscillates in size with large amplitude due to $r_{0\mathrm{h}} < r_{\mathrm{m}}$, the back of the pulse is well-confined. (b) On-axis density is reduced due to heating. (c) Spot size of a low-power probe pulse with wavelength 815 nm, showing good guiding a few ns after the peak of the heater pulse.

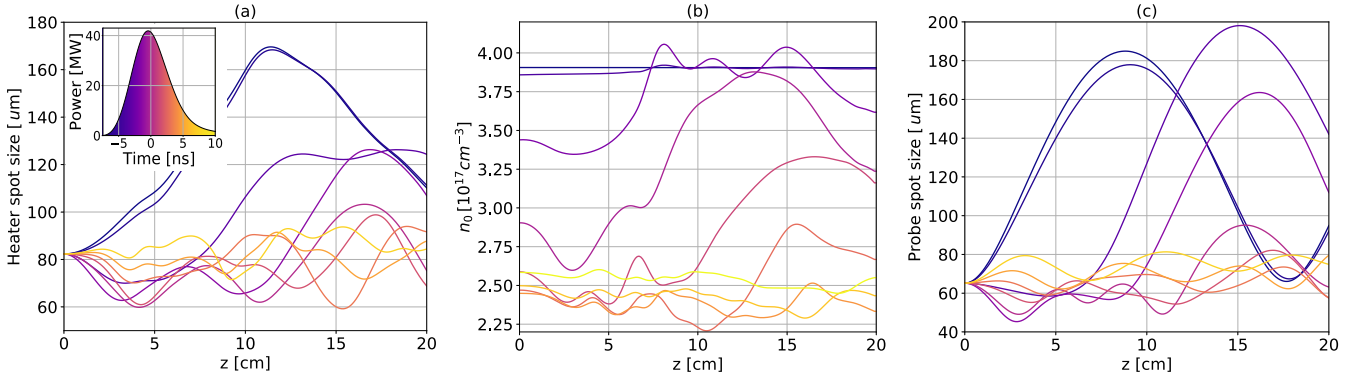

FIG. 4. Simulation of channel formation for heater pulse arrival 440 ns after the peak of the discharge pulse and initial hydrogen atomic density $6.12 \times 10^{17}\mathrm{cm}^{-3}$. Inset of (a): Temporal profile of the heater pulse with energy 0.3 J, with the color scale indicating the temporal slice for subsequent plots. The dark blue and orange colors correspond to the front and back slices of the heater pulse, respectively. (a-c) show laser and channel properties for different time slices 2 ns apart as a function of propagation distance z. The heater pulse near field (at the focusing lens) profile was taken to be top hat. (a) Spot size of the heater pulse. While the front of the pulse oscillates in size with large amplitude due to $r_{0\mathrm{h}} < r_{\mathrm{m}}$, the back of the pulse is well-confined. (b) The on-axis density is reduced more than for Fig. 3 due to a lower pre-heater plasma temperature that increased heating rate. (c) Spot size of a low-power probe pulse with wavelength 815 nm, showing lower spot sizes than for Fig. 3 and hence the production of a channel with lower r_{m}.

mittivity $\varepsilon = \varepsilon' + i\varepsilon''$. The heating rate, according to Ref. [29] in Kramers approximation, is given by

$$R = I\frac{2\pi\varepsilon''}{\lambda_h} = \frac{2^{5/2}\pi^{1/2}}{3}\frac{zq_e^4 n_i I}{m_e^{1/2}T_e^{3/2}}\frac{\omega_{pe}^2}{\omega_{\mathrm{h}}^2}\Lambda\,, \qquad (1)$$

where q_{e} and m_e are the electron charge and mass, n_i is the ion density, z the ion charge number, ω_{pe} is the electron plasma frequency, and $\omega_{\mathrm{h}} = 2\pi c/\lambda_{\mathrm{h}}$ is the frequency of the heating laser, with the Coulomb logarithm given by

$$\Lambda = \max\left\{\frac{\pi}{3^{1/2}},\ \frac{1}{2}\ln\left[\frac{2^5 T_e^3}{\exp\left(5C_\gamma\right)\omega_h^2 z^2 q_e^4 m_e}\right]\right\}, \qquad (2)$$

where $C_\gamma = 0.57721...$ is the Euler-Mascheroni constant. This expression for the rate of plasma heating due to the absorption of the laser pulse energy via the inverse bremsstrahlung process is valid, when $T_e \ll z^2 e^4 m_e/\hbar^2 \sim 27z^2$ eV, and $\omega_h \gg \omega_{pe}$. In the regime treated here, with heater intensities below 10^{12} W/cm^2,

the heating rate dependence can be simplified to:

$$R \propto \frac{n_i I \lambda_{\rm h}^2}{T_e^{3/2}}. \quad (3)$$

According to this estimation, typical temperature changes near peak laser intensity in the experiments presented here are expected to be of order 1 eV/ns. Using nanosecond-scale heater pulses, this can induce significant heating in hydrogen discharge plasmas that typically have temperature distributions peaking at a few eV [25].

Both the plasma channel formation from the discharge and the channel modification through IB heating were modeled with the multi-dimensional code MARPLE (Magnetically Accelerated Radiative PLasma Explorer) [30–32], with the laser heating rate calculated using equations 1 and 2. Additional modules from INF&RNO [33, 34] were used to calculate the heater laser pulse propagation. An example of this taken from Ref. [20] is shown in Fig. 2. The temperature rises with the current through Ohmic heating. The density rises through ionization and drops through channel formation. After the peak of the current the temperature drops due to reduced Ohmic heating and cooling at the capillary wall. The heater laser pulse with duration 8 ns full-width-half-maximum (FWHM) arrived 300 ns after the peak of the discharge current, at which point the temperature rises from 4.1 to 4.7 eV, resulting in a reduction in on-axis density, indicating the lowering of $r_{\rm m}$. Since the ion acoustic speed is tens of micron per ns, later temporal slices of the heater pulse encounter a plasma channel that is already deepened by preceding slices. Because subsequent slices propagate through stronger plasma channels, employing a longer pulse has the advantage that the heater pulse focused spot size need not be initially matched to the plasma channel. This allows for a tighter focus of the heater pulse, and hence, reduced $r_{\rm m}$ after heating.

Due to the evolution of the heater pulse as a function of propagation distance in these experiments, the density profile is expected to have longitudinal modulations. This was investigated with MARPLE simulations. The heater laser pulses had wavelength $\lambda_{\rm h} = 532\,$nm, energy 300 mJ, FWHM duration 8 ns, and focused spot size $r_{0\rm h} = 82\,\mu$m. The capillary discharge current pulse used was experimentally measured, and shown in Fig. 2 to have an amplitude of 450 A and rise time of 400 ns. The capillary had diameter 800 μm and length 20 cm. The initial hydrogen atomic density was 6.12×10^{17} cm^{-3}. In the simulations we do not take into account density distribution near the ends of the capillary. Although the heater thermal self-focusing will change with more accurate modeling of the density ramp between the capillary ends and the gas inlets, the effect is expected to be small since the ramp length of $\approx 6\,$mm [31] is less than the Rayleigh range of 4 cm. The heater pulse temporal profile is shown in the inset of Fig. 3(a), and the color is used to show the temporal location for subsequent plots. It should be noted that compared to simulations presented in Ref. [20] that employed a heater pulse with Gaussian spatial profile, the new simulations in this work use a profile that is top-hat at the focusing lens and is a closer approximation of the experimental heater pulse mode.

As the heater propagates through the channel, the first temporal slices are initially poorly confined, as evidenced by the large spot size evolution of the blue curves in Fig. 3(a), which is for heater arrival 320 ns after the peak of the discharge. Here the spot size is defined as the second moment within a radius of 160 μm. This definition of spot size allows for a better measure of guiding efficacy for the case of non-Gaussian laser pulses. The temporal slice of the heater pulse guided best over the 20 cm length is a few ns after the peak, with spot size variation between 70 and 90 μm (orange curves), indicating that 8 ns is a reasonable choice of pulse length. Guiding of the heater pulse is important because increased heating over a smaller area around the axis more efficiently causes expansion of a narrow heated column. Propagation of the early time slices of the heater pulse is determined mainly by the plasma channel formed in the capillary discharge before the heater, whereas propagation of the majority of the heater pulse is governed additionally by the modification of the plasma channel due to laser heating. Both these effects determine complicated longitudinal and temporal structure of the heater laser pulse shown in Figures 3(a) and 4(a). The density is also lowest a few ns after the peak of the heater pulse, as shown in Fig. 3(b), with axial variation between 2.82 and 3.02×10^{17}cm^{-3}. It should be noted that for timing at the peak of the heater pulse, the longitudinal variations are larger. This may explain the observation in Ref. [20] that a larger portion of charge at low energy was measured in experiments compared with simulations that employed a heater pulse with a Gaussian spatial profile. Further particle in cell (PIC) simulations are needed to evaluate the effect of these larger density oscillations, but it is reasonable to expect that the increased density near the center of the capillary will introduce additional low energy charge, as observed in the experiments (Fig. 1). A high degree of uniformity can be achieved about 7 ns after the peak of the heater pulse, with density variation between 2.87 and 2.99×10^{17}cm^{-3}.

In order to evaluate the efficacy of the guiding structure created for the laser pulse spot size employed in the high power experiments of Fig. 1, the evolution of a probe pulse with focal spot size $r_0 \approx 63\,\mu$m was simulated. The wavelength was 815 nm and the power low such that ionization effects could be neglected. As shown in Fig. 3(c), the best confinement of the pulse is observed for the lowest density channel, with modest fluctuations in spot size. This means that in high power experiments the peak intensity and accelerating field is expected to remain high throughout the capillary. In summary, Fig. 3 shows that although the front of the heater pulse was mismatched to the plasma channel, later temporal slices of the pulse could be propagated with just $\approx 10\,\%$ change in spot size, forming a channel with reduced density and $r_{\rm m}$ over the

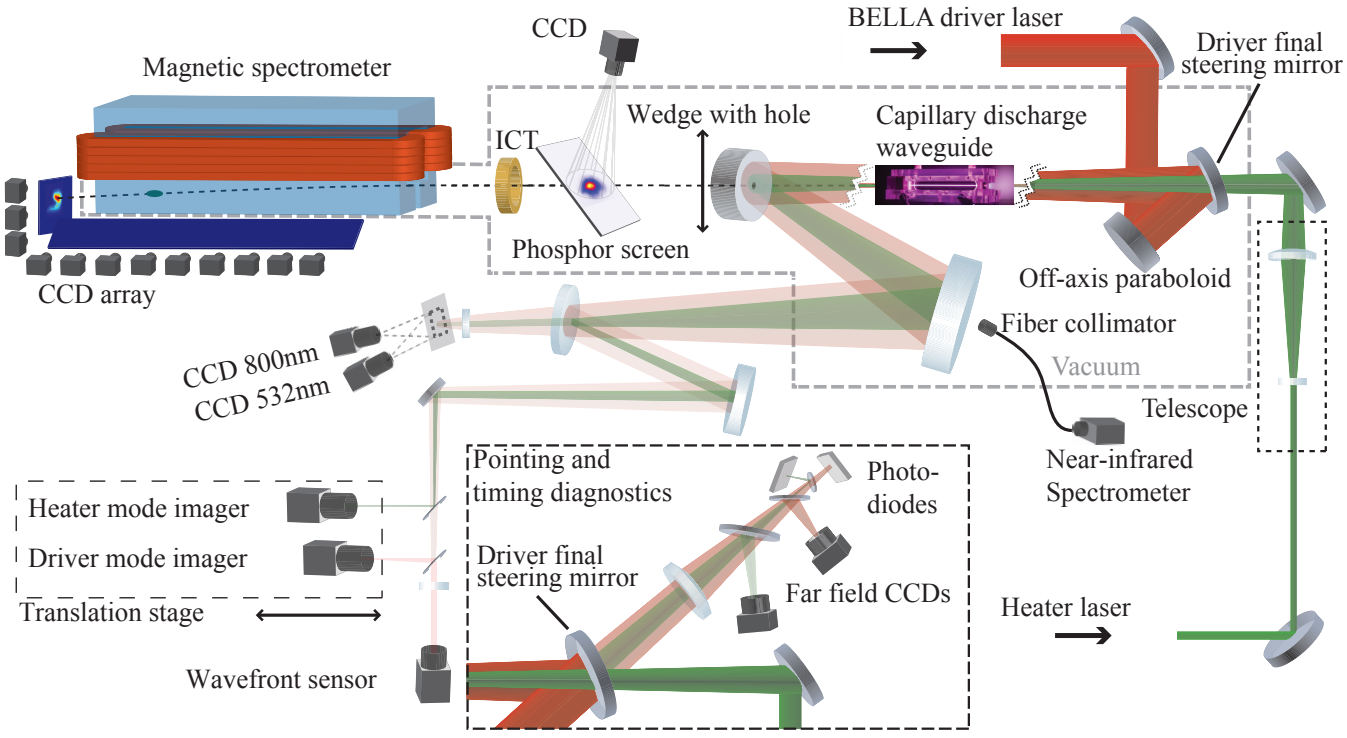

FIG. 5. Schematic of the experimental setup showing the target and diagnostics of the laser and electron beam. Figure taken from A. J. Gonsalves et al, Physical Review Letters 122, 084801 (2019) [20].

entire length of the capillary.

The experiments in Ref. [20] showed that stronger low density channels could be achieved by operating the heater pulse later in the discharge. This was due to the increased laser heating associated with initially colder plasma channels. Here we model these effects with an MHD simulation (Fig. 4) with heater pulse arrival 440 ns after the peak of current. Again excellent guiding of the heater pulse is observed ≈5 ns after the peak, as shown in Fig. 4(a), while earlier temporal slices undergo significant spot size oscillation. In contrast to the case for 320 ns delay, however, excellent guiding is observed all the way to the tail of the pulse (yellow curve). Channels with longitudinal density uniformity better than 10 % are observed from about 5 ns in Fig. 4(b), with channel density variation between 2.27 and $2.47\times10^{17}\mathrm{cm}^{-3}$ for time 6 ns. This larger density reduction observed for the colder pre-heater plasma (Fig. 4 vs. Fig. 3) is important for maximizing electron beam energy in the LPA. The lower density is achieved simultaneously with the generation of a sufficiently deep channel, with excellent confinement of the Gaussian probe pulse shown in Fig. 4(c).

III. CHANNEL FORMATION EXPERIMENTS

A. Guiding of the heater pulse

In order to demonstrate the heater self-focusing predicted in Fig. 3, heater guiding experiments were performed at the BELLA petawatt facility [35], with the setup shown in Fig. 5. The heater and discharge pulse parameters were chosen to be the same as the simulation of Fig. 3 (e.g. $r_{0\mathrm{h}} = 82\,\mu\mathrm{m}$), except for heater pulse energy, which was varied. The capillary length was chosen to be 9 cm instead of the 20 cm used in high power experiments [20] so that the output spatial modes would be a more sensitive diagnostic of guiding and avoid confusion between matched and unmatched guiding when a small output laser mode is observed. This can be seen from Fig. 3(a), where the front of the heater pulse (that is minimally affected by IB heating) has a large output mode after 9 cm of propagation. This can be contrasted with the output mode size at 20 cm, which appears well guided for the low power leading slice of the pulse even when a large spot size oscillation occurs. The heater laser pulses at the entrance and exit of the capillary were imaged using a CCD camera and an all-reflective achromatic telescope with three uncoated wedges. A CCD camera was also used to image the location of the first uncoated wedge for alignment and near field beam profiling. A photodiode and Pearson coil measured the tem-

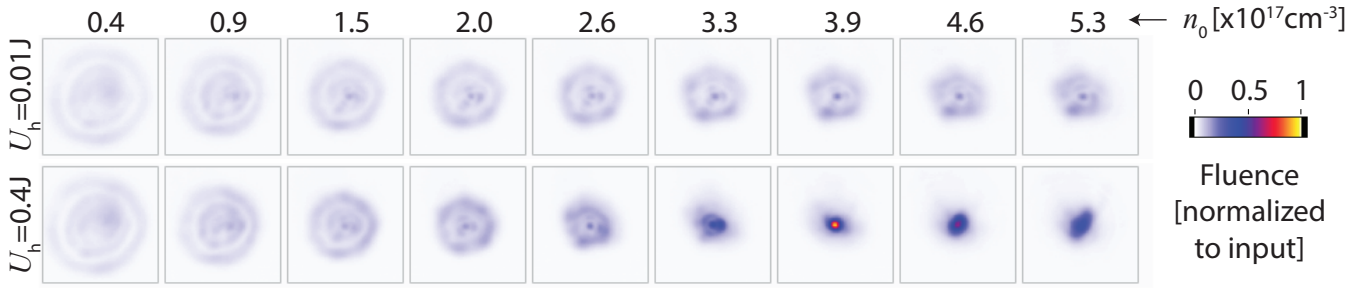

FIG. 6. Heater pulse output modes vs initial on-axis density (labeled above the images in units of $\times 10^{17}\mathrm{cm}^{-3}$), for a 90 mm capillary. The heater pulse energy is shown on the left of each image row. The images have a field of view of 700 μm x 700 μm. The effect of self-guiding of the heater is clear for increasing initial density, with significant reduction in spot size.

poral evolution and timing of the heater and discharge pulses, respectively.

Heater pulse spatial profiles at the exit of the capillary are shown in Fig. 6 as a function of plasma density. The top row is for laser energy 0.01 J, for which the effects of laser heating are negligible. As plasma density is increased, the mode size decreases since the matched spot size of the channel created by the discharge decreases as $r_\mathrm{m} \propto n_0^{-1/4} D_\mathrm{cap}^{1/2}$ [25, 36]. The bottom row is for laser energy 0.4 J. At density $\approx 0.4\times10^{17}\mathrm{cm}^{-3}$, there is negligible effect of increasing the heater pulse energy, demonstrating that there is no self-guiding effect. As the density is increased, the heating rate increases according to Eq. 3 and laser heated channels with lower r_m are produced, leading to smaller mode size and higher peak fluence. The fact that the heater pulse mode size is reduced for high compared with low heater laser pulse energy is due to the thermal self-focusing effect shown in the simulations of Fig. 3(a). Early temporal slices of the heater pulse created subsequently deeper plasma channels that guided later slices of the heater pulse.

B. Guiding of a low power probe pulse

In order to directly probe the channel temporal evolution due to IB heating, “driver" laser pulses from the BELLA petawatt laser at a wavelength $\lambda = 815\,\mathrm{nm}$ with spectral width 40 nm were focused to a focal spot size $r_0 \approx 60\,\mu\mathrm{m}$ by a 13.5 m focal length off-axis parabolic mirror onto the entrance of a capillary waveguide as shown in Fig. 5. The laser pulses were stretched to $\tau_0 \simeq$ 1.5 ps full-width-half-maximum (FWHM) and attenuated to driver energy $U_\mathrm{d} = 26$ mJ so that ionization, relativistic self-focusing, and wake generation could be neglected.

For times before the heater pulse arrival (<-10 ns before the peak of the heater pulse at 0 ns), the output probe size is constant over the times sampled. A typical output mode taken 20 ns before the peak of the heater pulse is shown at the top left of Fig. 7. At -5 ns, which corresponds to the rising edge of the heater pulse, the effect of the heater is apparent from an increase in fluence

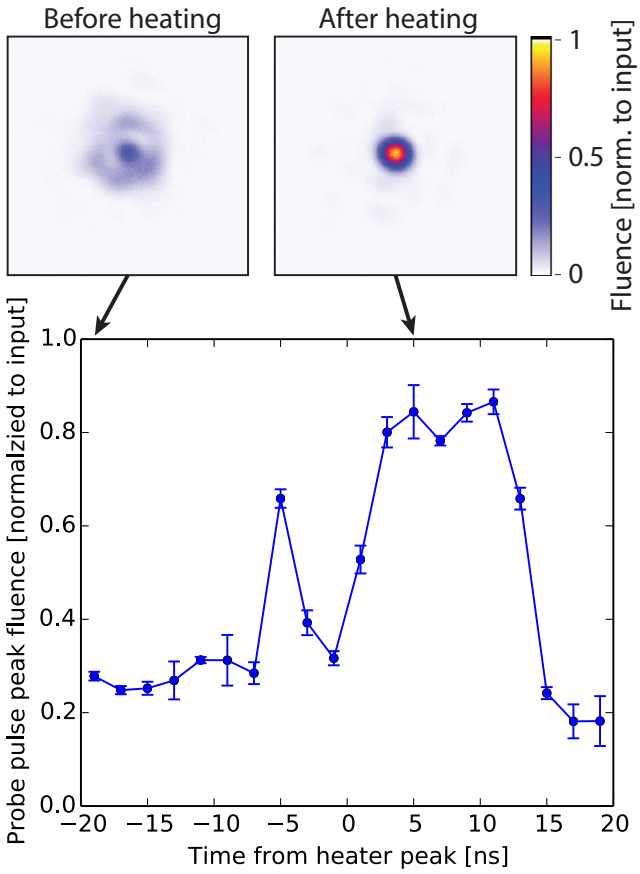

FIG. 7. Probe pulse output fluence vs time from heater peak for pre-heater on-axis electron density $3.5 \times 10^{17}\mathrm{cm}^{-3}$ and heater pulse energy 0.4 J, after propagation through a 90 mm capillary. Example output modes are shown with field of view of 700 μm x 700 μm. The reduction in spot size and corresponding increase in fluence demonstrate improved guiding with the heater pulse.

at the capillary exit, followed by an oscillatory behavior. This is due to the changing matched spot size and spot size oscillation period, as shown in Fig. 3(c) and Fig. 4(c). It should be noted that the details of the peak fluence lon-

gitudinal evolution depends strongly on the spatial mode of the probe pulse. In particular, laser pulses with top hat near field profile show stronger peak fluence oscillations. The fluence is maximized approximately 5 ns after the peak of the heater pulse, and a typical output mode is shown at the top right of Fig. 7. This reduction in spot size is also observed in the simulation shown in Fig. 4 at z=9 cm, cf. the orange curve (5 ns) compared to the blue curve (-7 ns).

C. Blueshift diagnostic of Ionization degree

Both MARPLE simulations (Fig. 3 and Fig. 4) and experiments of Ref. [20] show that the effect of the heater pulse is increased by operating later in the discharge pulse where the current and electron temperature are lower. In addition, these are the conditions for which the highest energy electron beam was observed. However, as the electron temperature is reduced, the plasma is no longer fully ionized. In order to demonstrate this experimentally, laser pulses with energy 33 mJ were compressed to 35 fs to enable ionization. Fig. 8(a) shows the ionization-induced blueshift wavelength vs. time in the discharge pulse. Here the blueshift wavelength is defined as the wavelength below which $1/e^2$ of the laser energy resides. As the current and plasma temperature increase, the increased ionization from the discharge reduces the amount of blueshifting (increases the blueshift wavelength). Between approximately the peak of the discharge pulse and 300 ns later the blueshift wavelength is constant, and there is negligible change from the input spectrum (dashed line). As the current and plasma temperature reduce, the spectrum shifts to shorter wavelength. The temporal evolution of the blueshift wavelength for heater pulse arrival 420 ns after the peak of the discharge pulse is shown in Fig. 8(b). The spectrum almost returns to the input spectrum at approximately 5 ns, demonstrating ionization due to the heater pulse. The trends observed in the experiment are consistent with the hydrogen ionization fraction obtained from the corresponding MARPLE simulation, which is shown in Fig. 8(c). The on-axis ionization fraction (red line) rises with increasing discharge current, has a plateau of full ionization for 500 ns, and falls as the current returns to 0. The heater pulse arrival at 440 ns can be seen by the rise again to full ionization. It should be noted that at larger radii the plasma is not fully ionized by the heater pulse. Future work will investigate the effect of this on guiding of high power laser pulses.

D. Redshift diagnostic of channel formation

Increasing the driver laser power further enables wakefield generation and redshifting of the laser spectrum. Figure 9(a) shows examples of redshifted spectra for increased laser power. This allows for a cross-check of the density and matched spot size measurements of Ref. [20] by comparing experimental and simulated laser spectra [19, 37]. Figure 9(b) shows the measured laser redshift versus laser energy for $n_0 = 3.2 \times 10^{17}$ cm^{-3} and $r_m = 68\,\mu$m (black diamonds). The redshift was defined as the wavelength above which $1/e^2$ of the signal was measured within the NIR spectrometer spectral window of 1050 nm to 1700 nm. Also shown are simulated values for the same conditions (black circles) obtained using the code INF&RNO after correcting for the instrument spectral response. These simulated values are in closer agreement with the experimental redshift than for simulations performed at lower (green) or higher (blue) density, and for smaller matched spot size (pink). These results suggest that the average plasma density is known to within approximately 10 percent. However it should be noted that from low power measurements day-to-day changes in the density for nominally identical conditions vary by about 10 %, most likely due to changes in the heater laser mode.

Laser-heated capillary discharge channels have been shown to generate beams up to 7.8 GeV using 850 TW of laser power, as was shown in Fig. 1 [20]. In this section, experiments provided a deeper understanding of how the plasma channel is formed and optimized. Thermal heater-self focusing was shown via guided mode measurements in which the heater guiding cannot be explained by the discharge-formed channel. Guiding of probe pulses provided insight into the temporal evolution of the laser-heated channel, with optimum guiding 5 to 10 ns after the peak of the heater pulse. For heater arrival late in the discharge pulse where the current is close to 0, the lowest density channels were produced, which is beneficial for maximizing electron energy gain in LPAs. Although the plasma is not fully ionized on-axis due to the discharge alone, MHD simulation shows that subsequent ionization due to the heater returns the ionization degree to 1 on-axis.

IV. MAXIMIZING ELECTRON BEAM ENERGY WITH A PETAWATT LASER

In this section we explore increasing the beam energy to 10 GeV via simulations using the code INF&RNO [33, 34]. The initial background plasma density profile is longitudinally uniform with 0.6 cm-long linear ramps at both ends of the capillary. The following expression was used as the initial condition for the BELLA laser pulse

$$\hat{a}(\zeta, r, t=0) = a_0 \,\mathrm{jinc}\left(\frac{r}{R_{jinc}}\right) f_{\parallel}(\zeta), \qquad (4)$$

where the field $\hat{a}(\zeta, r, t = 0)$ is the amplitude of the (complex) envelope of the normalized laser vector potential, t is the time, $\zeta = z - ct$ is the longitudinal co-moving coordinate (z being the longitudinal coordinate), r is the transverse coordinate (the simulations considered here are axisymmetric), the function

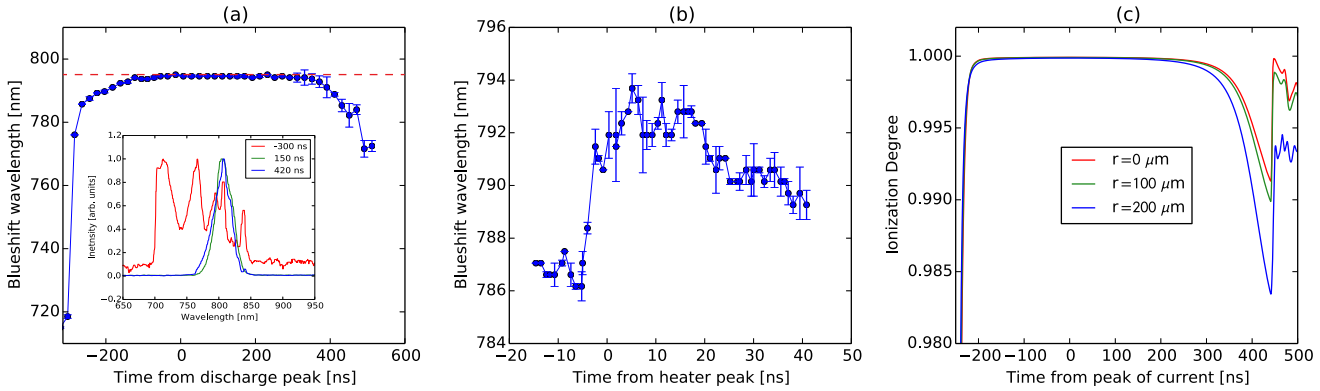

FIG. 8. Spectral edge of probe laser pulses with energy 33 mJ and pulse length 35 fs exiting a capillary of length 20 cm for $n_0 \approx 3.8\times10^{17}\mathrm{cm}^{-3}$. In (a) only the discharge is fired and the delay of the probe from the discharge peak is varied. The dashed red line corresponds to the value with the capillary removed from the beam path. The inset to (a) shows example spectra for time -300 ns (red), 150 ns (green), and 420 ns (blue). In (b) the delay of the probe from discharge peak is held constant at 420 ns, and the heater pulse timing is varied. The error bars correspond to the standard deviation of the measured data. The hydrogen ionization fraction from the MARPLE simulation of Fig. 4 is shown in (c) for the axial location (red), for 100um off axis (green), and for 200um off axis (blue). The steep rise in ionization at 440 ns is due to the arrival of the heater pulse.

jinc$(u) = 2J_1(u)/u$ [$J_1(u)$ being the first-order Bessel function of the first kind] describes the transverse laser field shape, $R_{jinc} \simeq 0.364r_0$, and the complex function $f_\parallel(\zeta)$ describes the experimentally-measured longitudinal laser temporal profile. We consider an LPA operating in the nonlinear regime, where particle production relies on self-injection. The physical parameters are as follows. The (post-heater) on-axis density is $n_0 = 2.2\times10^{17}$ cm^{-3}, and the matched radius $r_\mathrm{m} = 65$ μm, which is close to the parameters obtained in Fig. 4 for times > 5 ns after the heater peak. The laser had energy $U_0 = 39$ J, pulse duration is $\simeq 30$ fs (FWHM maximum of the intensity, the experimental profile is used), and $r_0 = 64\,\mu$m, yielding peak laser power 1.3 PW and $a_0 = 2.86$. The size of the computational box (2D $r-z$ axisymmetric) was $27k_p^{-1} \times 44k_p^{-1}$, where $k_p = \omega_p/c$. The longitudinal and transverse (radial) resolutions were, respectively, $k_p\Delta\zeta = 0.005$, and $k_p\Delta r = 0.033$, and the time step was $\omega_p\Delta t = 0.0012$. The number of numerical particles per cell was 6 for $k_p r \leq 5$, and then the number was decreased to 1 approaching the radial boundary. The simulation was run using a moving window with open boundary conditions in the longitudinal direction, and an absorbing boundary in the transverse direction. INF&RNO uses a fourth-order Runge-Kutta integrator for the temporal evolution of particles and fields [33], and a second-order implicit integrator for the laser envelope [34]. The simulation cost for this run was $\sim$ 120,000 core hours (88 hours on 1350 cores) on the Edison supercomputer at the National Energy Research Scientific Computing Center (NERSC), an estimated reduction of a factor $\gtrsim 100$ compared to simulations performed with conventional 3D PIC codes.

The laser-plasma parameters were chosen to be slightly above the threshold for particle self-injection [38]. This helped improve the spectral properties of the accelerating bunch by preventing continuous injection of charge. Additional constraints in the choice of the parameters came from the requirement that the laser must remain well guided over the 20 cm of the plasma, and that the laser depletion length is comparable to the dephasing length. The plasma density profile was taken to be uniform between the gas inlets and linear between the gas inlets and the capillary ends. Since the ramp length is approximately the distance between the gas inlet and capillary end [31], and this distance is less than the Rayleigh range of the laser pulse, the precise shape of the ramp is expected to have only a small effect on laser propagation. For example, in the paraxial approximation, the maximum difference in peak fluence between a linear ramp and a more realistic square root dependence ramp was less than 5 %.

In Fig. 10 (a) we show (red solid line) the evolution of the peak value of the normalized laser vector potential as a function of the propagation distance in the plasma (the black line represents the on-axis density profile), demonstrating that good guiding of the laser is achieved. The LPA operates in the nonlinear regime, but, contrary to the bubble regime, the laser does not self-guide without the plasma channel (blue dashed line). The laser intensity increased above the initially focused value due to the effects of self-focusing and self-steepening of the laser pulse. Efficient laser guiding was achieved, meaning that the laser intensity remained higher than the vacuum focal value.

Modeling shows that background electrons are self-injected and accelerated in the laser-driven wake. Most of self-injection occurs for $z \lesssim 10$ cm. In Fig. 10 (b) we show the electron beam energy spectrum at the exit of the LPA. In computing the spectrum we considered

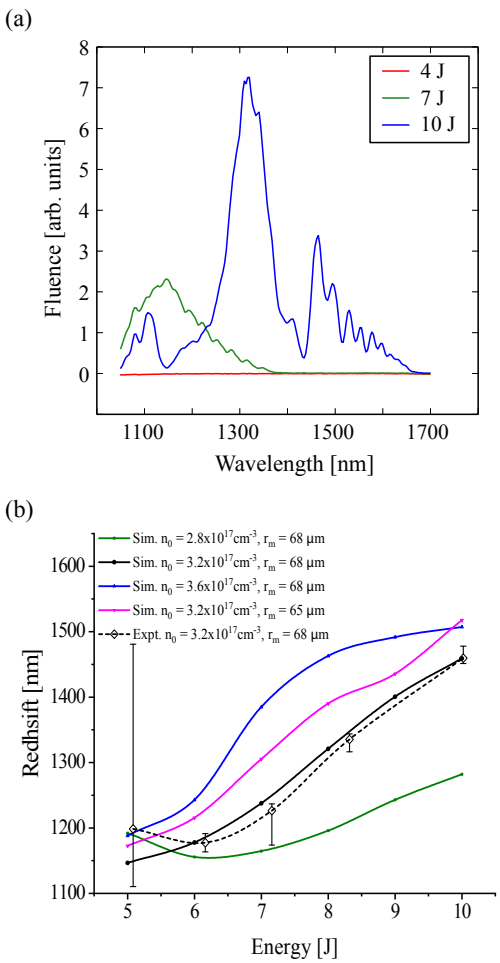

FIG. 9. (a) Example drive laser spectra at the exit of the waveguide for input laser energy 4 J (red), 7 J (green) and 10 J (blue). (b) Redshift vs. laser energy on target for experiment and simulation. The experiment result (black diamonds) is well matched to the simulated result (black circles). The error bars correspond to the quarter percentiles of the data. Simulation for higher density (blue) showed higher redshift than experiment and simulation for lower density (green) showed lower redshift. Simulation for the experimental density but lower $r_{\rm m}$ (pink) showed higher redshift, due to increased confinement of the laser pulse.

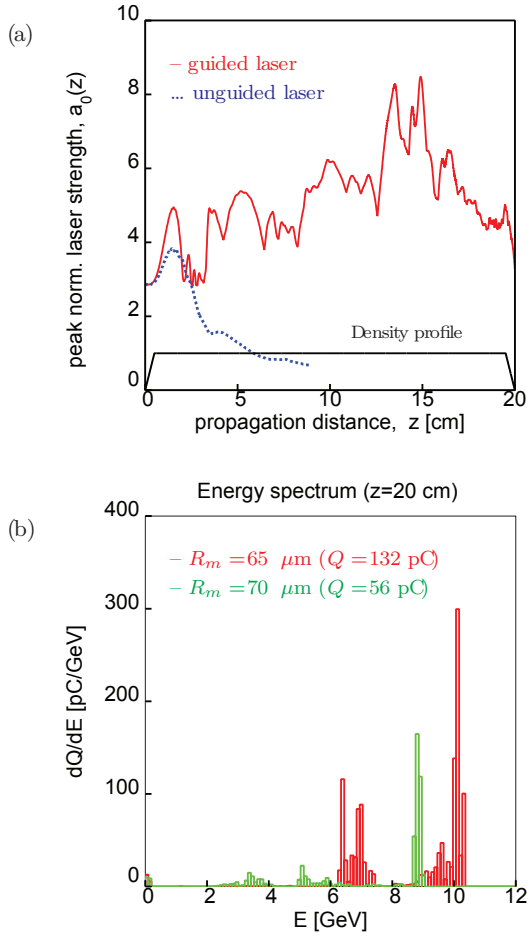

FIG. 10. (a) Evolution of the peak value of the normalized laser vector potential as a function of the propagation distance for a guided (red solid) and an unguided (blue dashed) laser in a 10 GeV-class LPA. The black line represents the on-axis density profile. The plasma parameters are $n_0 = 2.2 \times 10^{17}$ cm^{-3}, $r_m = 65$ μm. The laser parameters are $U = 39$ J, $w_0 = 64$ μm, and $T_0 = 30$ fs (FWHM of the intensity). (b) Electron beam energy spectrum measured at the exit of the LPA ($z = 20$ cm, self-injection) for different values of the matched radius, $r_{\rm m} = 65$ μm (red) and $r_{\rm m} = 70$ μm (green). The accelerated charge is 132 (56) pC for $r_{\rm m} = 65(70)$ μm.

only the particles within the angular acceptance of the BELLA spectrometer (i.e., ± 1 mrad). The accelerated charge is 132 pC, and the charge in the high-energy quasi-monoenergetic feature of the spectrum (average energy 9.9 GeV, rms relative energy spread 4%, rms divergence 0.26 mrad) is 80 pC. It should be noted that the exit density ramp has negligible effect on the high energy part of the bunch since the betatron period of the bunch is longer than the ramp itself, and the wake amplitude is reduced as the laser intensity decreases in the ramp. However, the presence of the down ramp at the exit of the capillary results in additional self-injection of relatively low energy particles (< 100 MeV) with very high divergence. Due to the limited acceptance of the magnetic spectrometer only ≈ 1 pC of this charge is captured, as shown in Fig. 10(b).

We also ran different simulations considering variations in the plasma parameters with respect to the proposed working point in order to assess the sensitivity of the final bunch properties to these parameters. The exploration of the parameter space is made possible by the (relatively) low computation cost of these simulations with INF&RNO. In particular, we considered a set of simulations where the matched radius was increased from 65 μm to 70 μm, 75 μm, and 80 μm. Simulations show that, as the matched radius increases, both the accelerated charge and the maximum bunch energy decrease. For instance,

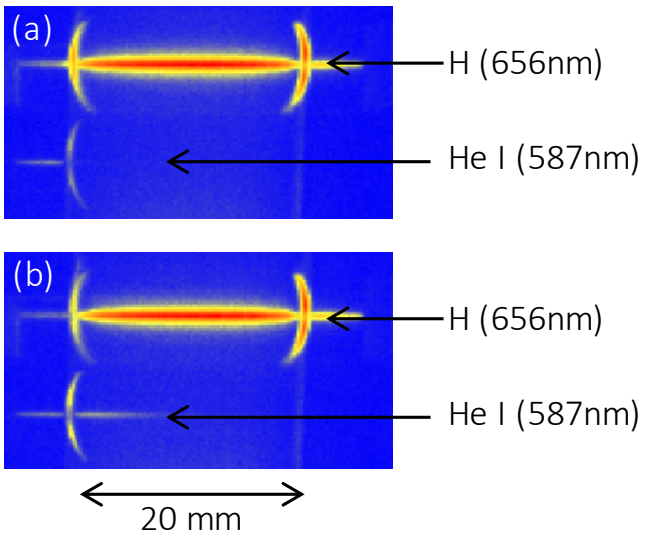

FIG. 11. Spectrally resolved images of the capillary discharge, showing the ability to control the length of mixed gas region for ioninization injection. The pressure at the intersection of the entrance gas inlet and the capillary was set to 20.4 Torr. The pressure at the intersection between the exit gas inlet and the capillary was set to 20.1 Torr for (a) and 19.4 Torr for (b).

for $r_{\rm m} = 75$ μm the maximum bunch energy was $\lesssim 8$ GeV (with a broad energy spread), and the final bunch charge was 10 pC. No bunch at the exit of the LPA was observed for $r_{\rm m} > 75$ μm. High-sensitivity of the final bunch parameters to the changes in the on-axis density was also observed in lower resolution simulations. These simulations show that 10 GeV electron beam single stage energy gain can be achieved with an increase in laser power to 1.3 PW, and density reduction to $n_0 = 2.2 \times 10^{17}$ cm^{-3} while maintaining a low matched radius $r_{\rm m} = 65$ μm. This motivates further laser-heater optimization, which could include optimization of heater laser spot size and wavelength.

V. CONTROLLING ELECTRON INJECTION

The electron beam produced in both the experiments and simulations of the previous sections showed electron beam spectra with multiple quasi-monoenergetic peaks, and the simulations show sensitivity to input parameters at the level of available control. The sensitivity is due in large part to the self injection process used [1]. In order to produce higher-quality and stable monoenergetic electron bunches both for single stage applications and multi-stage LPAs, injection must be controlled in addition to the laser propagation. Methods requiring additional laser pulses promise to produce beams of unprecedented quality [39, 40]. Here we begin the investigation of controlled injection in multi-GeV LPAs with ionization injection using the drive laser pulse, as was done for lower beam energies [41].

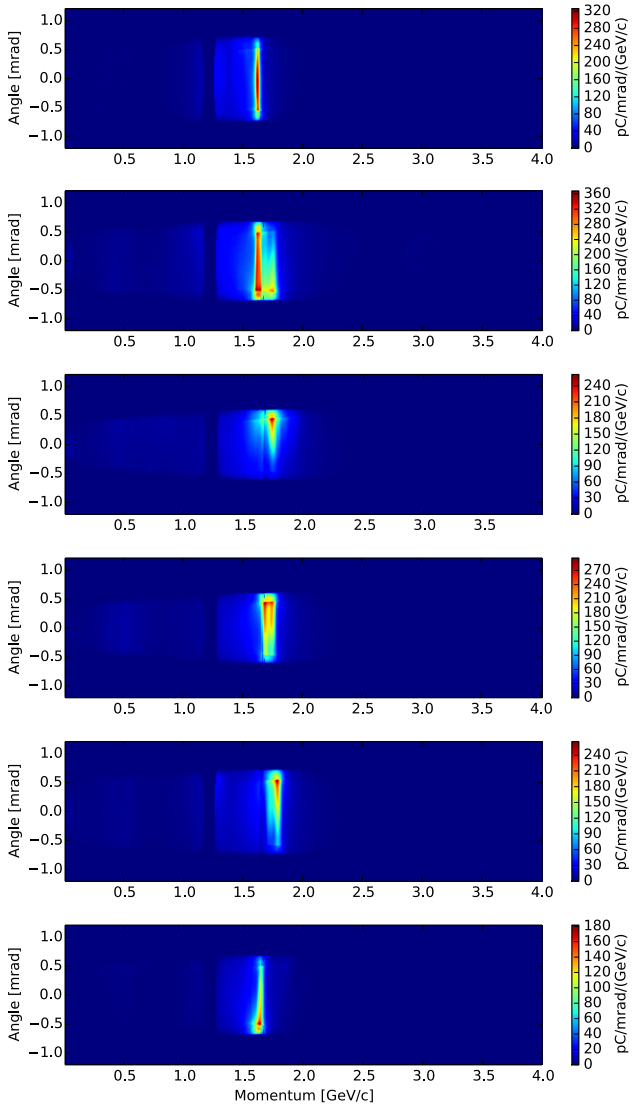

FIG. 12. Example electron beam spectra produced in a capillary discharge waveguide filled with 1 % nitrogen, balance helium in the front of the capillary, and hydrogen in the remainder of the capillary. The capillary had length 3.3 cm and diameter 0.5 mm, and the plasma density was $n_0 = 7 \times 10^{17}$ cm^{-3}. The laser, which had a vacuum focal spot of 53 µm was focused 1.3 cm into the capillary, with energy 17 J, and pulse length 35 fs.

Previous experiments using the capillary discharge for LPAs saw evidence for ionization injection [42], but the species, concentration, and length of the dopant region were not controlled. Here we show that the length of a mixed gas region can be controlled by introducing the dopant species that provides the electrons to be injected in the entrance gas inlet of a capillary and adjusting the pressure relative to the pressure at the downstream gas inlet. This is shown for helium gas with dopant 0.5 %

N_2 in Fig. 11 with spectrally resolved images similar to those in Ref. [43]. The horizontal lines in each image correspond to the capillary, the upper one corresponding to hydrogen and the lower to helium. The vertical curved lines above the capillary correspond to the gas inlets, and the curved lines below the capillary lead to a capacitance manometer used for pressure measurement. He was chosen as the balance of the dopant gas since it allows for determination of the length of the dopant region. It should be noted that He is not fully ionized and the transverse density profile in this region will be different. For higher electron energy that requires efficient guiding in a longer plasma channel, hydrogen should be used, or the length over which dopant gas be limited to less than a Rayleigh range. In Fig. 11(a) the pressure at the upstream inlet-capillary intersection is 0.3 Torr lower than for the downstream counterpart. This results in a well localized region of the helium nitrogen mixture. In Fig. 11(b) the pressure at the exit inlet/capillary intersection was reduced to 19.4 Torr, and the mixed gas region approximately doubled in length. It should be noted that the images in Fig. 11 are time integrated and do not provide a quantitative density profile of the hydrogen or dopant species. However they do demonstrate the ability to localize the dopant gas within the capillary discharge waveguide.

For electron beam generation experiments the first optical wedge was translated so that the hole was in the beam path, allowing electrons to propagate to the electron beam diagnostics shown in Fig. 5. The electron beam energy was measured using a 2.5 m-long magnetic spectrometer (tunable up to 1.2 T) by imaging two phosphor screens of length 0.2 m and 2.5 m at the exit plane of the spectrometer onto 12 CCD cameras. In order to separate the challenges of controlled injection and guiding over the distances required for ≈10 GeV energy gain, the electron beam generation experiments were performed in a capillary of length 3.3 cm, which is shown in Fig. 11. Over this length self-guiding is effective, and the laser heater pulse was not required. The laser for these experiments had energy 17 J and pulse length 35 fs, and was focused 1.3 cm past the entrance of the capillary. The dopant region was localized to the first $\approx 1\,$cm of the capillary and the plasma density set to $n_0 \approx 7 \times 10^{17}$ cm^{-3}.

Example electron beams, chosen based on those that were best aligned to the magnetic spectrometer, are shown in Fig. 12. For density 65 % of that shown in Fig. 12, which is near the threshold for electron injection, the charge was sensitive to mm changes in the laser focal location. For the shots shown in Fig. 12, the charge was 45 pC±16 pC, and the peak energy was 1.66 GeV±0.06 GeV. In total 50 shots were taken for these parameters and 12 shots were pointed with sufficient accuracy to be measured by the magnetic spectrometer. For these 12 shots the charge and peak energy were 44 pC±13 pC and 1.7 GeV±0.1 GeV, respectively. The best centered beam (top) had energy 1.6 GeV, charge 38 pC, divergence 1 mrad FWHM, and energy spread less than 2 % (resolution limited). Beams with such low energy spread are ideal for staged acceleration experiments, where low energy spread is required for high efficiency transport and capture in the second stage [44].

VI. CONCLUSION

IB heating inside a capillary discharge waveguide increased the channel depth and enabled the guiding of petawatt laser pulses at low density ($\approx 3 \times 10^{17}\,$cm^{-3}) over $\approx 15\ Z_{\rm R}$. Simulations were presented, showing how the plasma channel is formed and the crucial role thermal self-focusing plays in generating low density channels with strong focusing force over the full length of the accelerator. Self-focusing of the heater pulse was confirmed with experiments in which the heater output mode was reduced as its energy was increased. Guiding of low power probe pulses shorter than the plasma evolution timescale showed optimum guiding 5-10 ns after the peak of the heater pulse, which was consistent with MHD and laser guiding simulations.

Since optimum channels (lowest density and strongest focusing forces) are observed for initially colder plasmas where ionization is incomplete and guiding may be impacted, guiding experiments were performed where the probe pulse intensity was large enough to ionize neutral hydrogen and introduce spectral shifts. The temporal evolution of blueshifting throughout the discharge and after arrival of the heater pulse were consistent with the evolution of the ionization degree seen in the MHD simulation, showing that the heater pulse fully ionizes the channel on-axis, which is beneficial for laser guiding.

Such plasma channels were used in experiments generating beams up to 7.8 GeV. Insight into the path toward increasing the beam energy further was gained via PIC simulations. Beams of energy 10 GeV were predicted by not only increasing laser power to 1.3 PW, but also reducing the plasma density further to $n_0 = 2.2 \times 10^{17}$ cm^{-3} while maintaining a channel with small matched spot size of $r_{\rm m} = 65\ \mu$m. MHD simulations suggest this is within reach of IB-heated capillary discharge waveguides, specifically by operating at later time within the heater pulse compared to previous experiments [20]. Both current experiments and these simulations of 10 GeV beams show energy spectra with multiple peaks. In order to inject a single electron bunch and generate a monoenergetic beam, work has begun on controlling injection in multi-GeV LPAs. We showed that beams with less than 2 % energy spread could be obtained by ionization injection over a localized region in a capillary discharge waveguide. This shows promise for future single-stage LPAs, and for high efficiency capture and acceleration in multi-stage LPAs.

VII. ACKNOWLEDGEMENTS

This work was supported by the Director, Office of Science, Office of High Energy Physics, of the U.S. Department of Energy under Contract No. DE-AC02-05CH11231 and DE-FG02-12ER41798, the Alexander von Humboldt Foundation, the project High Field Initiative (CZ.02.1.01/0.0/0.0/15_003/0000449) from the European Regional Development Fund, RFBR project number 20-31-70015, and NSF. The simulations used the computational resources of the national research scientific computing center (NERSC). The authors gratefully acknowledge the technical support from Zac Eisentraut, Dave Evans, Mark Kirkpatrick, Art Magana, Greg Mannino, Joe Riley, Tyler Sipla, Austin Bajema, Jonathan Bradford, Will Waldron, Gregory Scharfstein, Don Syversrud and Nathan Ybarrolaza. The authors would also like to thank Eric Colby and Dieter Waltz for assistance with the magnetic spectrometer. The contributions of WPL to this research occurred prior to his new position at DESY on Feb 1, 2019.

[1] E. Esarey, C. B. Schroeder, and W. P. Leemans, Rev. Mod. Phys. **81**, 1229 (2009).
[2] S. M. Hooker, Nat. Photonics **7**, 775 (2013).
[3] M. Fuchs, R. Weingartner, A. Popp, Z. Major, S. Becker, J. Osterhoff, I. Cortrie, B. Zeitler, R. Hörlein, G. D. Tsakiris, U. Schramm, T. P. Rowlands-Rees, S. M. Hooker, D. Habs, F. Krausz, S. Karsch, and F. Grüner, Nat. Phys. **5**, 826 (2009).
[4] Z. Huang, Y. Ding, and C. B. Schroeder, Phys. Rev. Lett. **109**, 204801 (2012).
[5] A. R. Maier, A. Meseck, S. Reiche, C. B. Schroeder, T. Seggebrock, and F. Grüner, Phys. Rev. X **2**, 031019 (2012).
[6] A. Loulergue, M. Labat, C. Evain, C. Benabderrahmane, V. Malka, and M. E. Couprie, New J. Phys. **17**, 023028 (2015).
[7] T. André, I. A. Andriyash, A. Loulergue, M. Labat, E. Roussel, A. Ghaith, M. Khojoyan, C. Thaury, M. Valléau, F. Briquez, F. Marteau, K. Tavakoli, P. N'Gotta, Y. Dietrich, G. Lambert, V. Malka, C. Benabderrahmane, J. Vétéran, L. Chapuis, T. El Ajjouri, M. Sebdaoui, N. Hubert, O. Marcouillé, P. Berteaud, N. Leclercq, M. El Ajjouri, P. Rommeluère, F. Bouvet, J. P. Duval, C. Kitegi, F. Blache, B. Mahieu, S. Corde, J. Gautier, K. Ta Phuoc, J. P. Goddet, A. Lestrade, C. Herbeaux, C. Évain, C. Szwaj, S. Bielawski, A. Tafzi, P. Rousseau, S. Smartsev, F. Polack, D. Dennetière, C. Bourassin-Bouchet, C. De Oliveira, and M.-E. Couprie, Nat. Commun. **9**, 1334 (2018).
[8] K. Ta Phuoc, S. Corde, C. Thaury, V. Malka, A. Tafzi, J. P. Goddet, R. C. Shah, S. Sebban, and A. Rousse, Nat. Photonics (2012), 10.1038/nphoton.2012.82, arXiv:1301.3973.
[9] C. G. Geddes, S. Rykovanov, N. H. Matlis, S. Steinke, J. L. Vay, E. H. Esarey, B. Ludewigt, K. Nakamura, B. J. Quiter, C. B. Schroeder, C. Toth, and W. P. Leemans, Nucl. Instruments Methods Phys. Res. Sect. B Beam Interact. with Mater. Atoms **350**, 116 (2015).
[10] K. Khrennikov, J. Wenz, A. Buck, J. Xu, M. Heigoldt, L. Veisz, and S. Karsch, Phys. Rev. Lett. **114**, 195003 (2015).
[11] T. W. Huang, C. M. Kim, C. T. Zhou, M. H. Cho, K. Nakajima, C. M. Ryu, S. C. Ruan, and C. H. Nam, New J. Phys. **21**, 0133008 (2019), arXiv:1803.08237.
[12] N. D. Powers, I. Ghebregziabher, G. Golovin, C. Liu, S. Chen, S. Banerjee, J. Zhang, and D. P. Umstadter, Nat. Photonics **8**, 28 (2014).
[13] W. Leemans and E. Esarey, Phys. Today **62**, 44 (2009).
[14] C. B. Schroeder, E. Esarey, C. G. R. Geddes, C. Benedetti, and W. P. Leemans, Phys. Rev. Spec. Top. - Accel. Beams **13**, 101301 (2010).
[15] B. Cros and P. Muggli, in *Rep. Adv. Nov. Accel. High Energy Phys. Roadmap Work.* (CERN, Geneva, 2017).
[16] X. Wang, R. Zgadzaj, N. Fazel, Z. Li, S. A. Yi, X. Zhang, W. Henderson, Y.-Y. Chang, R. Korzekwa, H.-E. Tsai, C.-H. Pai, H. Quevedo, G. Dyer, E. Gaul, M. Martinez, A. C. Bernstein, T. Borger, M. Spinks, M. Donovan, V. Khudik, G. Shvets, T. Ditmire, and M. C. Downer, Nat. Commun. **4**, 1988 (2013).
[17] H. T. Kim, K. H. Pae, H. J. Cha, I. J. Kim, T. J. Yu, J. H. Sung, S. K. Lee, T. M. Jeong, and J. Lee, Phys. Rev. Lett. **111**, 165002 (2013).
[18] H. T. Kim, V. B. Pathak, K. Hong Pae, A. Lifschitz, F. Sylla, J. H. Shin, C. Hojbota, S. K. Lee, J. H. Sung, H. W. Lee, E. Guillaume, C. Thaury, K. Nakajima, J. Vieira, L. O. Silva, V. Malka, and C. H. Nam, Sci. Rep. **7**, 10203 (2017).
[19] W. P. Leemans, A. J. Gonsalves, H. S. Mao, K. Nakamura, C. Benedetti, C. B. Schroeder, C. Tóth, J. Daniels, D. E. Mittelberger, S. S. Bulanov, J. L. Vay, C. G. R. Geddes, and E. Esarey, Phys. Rev. Lett. **113**, 245002 (2014).
[20] A. J. Gonsalves, K. Nakamura, J. Daniels, C. Benedetti, C. Pieronek, T. C. H. D. Raadt, S. Steinke, J. H. Bin, S. S. Bulanov, J. V. Tilborg, C. G. R. Geddes, C. B. Schroeder, C. Tóth, E. Esarey, K. Swanson, G. Bagdasarov, N. Bobrova, V. Gasilov, G. Korn, P. Sasorov, W. P. Leemans, and L. Berkeley, Phys. Rev. Lett. **122**, 084801 (2019).
[21] C. G. Durfee III and H. M. Milchberg, Phys. Rev. Lett. **71**, 2409 (1993).
[22] D. J. Spence and S. M. Hooker, Phys. Rev. E **63**, 015401 (2000).
[23] W. P. Leemans, B. Nagler, A. J. Gonsalves, b. C. Tóth, K. Nakamura, C. G. R. Geddes, E. Esarey, C. B. Schroeder, and S. M. Hooker, Nat. Phys. **2**, 696 (2006).
[24] T. P. A. Ibbotson, N. Bourgeois, T. P. Rowlands-Rees, L. S. Caballero, S. I. Bajlekov, P. A. Walker, S. Kneip, S. P. D. Mangles, S. R. Nagel, C. A. J. Palmer, N. Delerue, G. Doucas, D. Urner, O. Chekhlov, R. J. Clarke, E. Divall, K. Ertel, P. S. Foster, S. J. Hawkes, C. J. Hooker, B. Parry, P. P. Rajeev, M. J. V. Streeter, and S. M. Hooker, Phys. Rev. ST Accel. Beams **13**, 031301 (2010).

[25] N. A. Bobrova, A. A. Esaulov, J.-I. I. Sakai, P. V. Sasorov, D. J. Spence, A. Butler, S. M. Hooker, and S. V. Bulanov, Phys. Rev. E **65**, 016407 (2001).

[26] N. A. Bobrova, P. V. Sasorov, C. Benedetti, S. S. Bulanov, C. G. R. Geddes, C. B. Schroeder, E. Esarey, and W. P. Leemans, Phys. Plasmas **20**, 20703 (2013).

[27] A. Y. Polishchuk and J. Meyer-Ter-Vehn, Phys. Rev. E **49**, 663 (1994).

[28] N. David, D. J. Spence, and S. M. Hooker, Phys. Rev. E **70**, 056411 (2004).

[29] E. M. Lifshitz and L. P. Pitaevskii, *Physical Kinetics* (Pergamon Press, Oxford, 2001).

[30] V. Gasilov, A. Boldarev, S. Dyachenko, O. Olkhovskaya, E. Kartasheva, G. Bagdasarov, S. Boldyrev, I. Gasilova, V. Shmyrov, S. Tkachenko, J. Grunenwald, and T. Maillard, Adv. Parallel Comput. **22**, 235 (2012).

[31] G. A. Bagdasarov, P. V. Sasorov, V. A. Gasilov, A. S. Boldarev, O. G. Olkhovskaya, C. Benedetti, S. S. Bulanov, A. Gonsalves, H.-S. Mao, C. B. Schroeder, J. van Tilborg, E. Esarey, W. P. Leemans, T. Levato, D. Margarone, and G. Korn, Phys. Plasmas **24**, 83109 (2017).

[32] G. Bagdasarov, P. Sasorov, A. Boldarev, O. Olkhovskaya, V. Gasilov, A. J. Gonsalves, S. Barber, S. S. Bulanov, C. B. Schroeder, J. van Tilborg, E. Esarey, W. P. Leemans, T. Levato, D. Margarone, G. Korn, and S. V. Bulanov, Phys. Plasmas **24**, 53111 (2017).

[33] C. Benedetti, C. B. Schroeder, E. Esarey, C. G. R. Geddes, and W. P. Leemans, in *Proc. 2010 Adv. Accel. Concepts Work.*, Vol. 1299, edited by G. Nusinovich and S. Gold (AIP, NY, 2010) pp. 250–255.

[34] C. Benedetti, C. B. Schroeder, C. G. Geddes, E. Esarey, and W. P. Leemans, Plasma Phys. Control. Fusion **60**, 014002 (2018).

[35] K. Nakamura, H.-S. Mao, A. J. Gonsalves, H. Vincenti, D. E. Mittelberger, J. Daniels, A. Magana, C. Toth, and W. P. Leemans, IEEE J. Quantum Electron. **53**, 1 (2017).

[36] A. J. Gonsalves, T. P. Rowlands-Rees, B. H. P. Broks, J. J. A. M. van der Mullen, and S. M. Hooker, Phys. Rev. Lett. **98**, 025002 (2007).

[37] S. Shiraishi, C. Benedetti, A. J. Gonsalves, K. Nakamura, B. H. Shaw, T. Sokollik, J. van Tilborg, C. G. R. Geddes, C. B. Schroeder, b. C. Tóth, E. Esarey, and W. P. Leemans, Phys. Plasmas. **20**, 63103 (2013).

[38] C. Benedetti, C. B. Schroeder, E. Esarey, F. Rossi, and W. P. Leemans, Phys. Plasmas **20**, 103108 (2013).

[39] L. L. Yu, E. Esarey, C. B. Schroeder, J. L. Vay, C. Benedetti, C. C. Geddes, M. Chen, and W. P. Leemans, Phys. Rev. Lett. **112**, 125001 (2014).

[40] C. B. Schroeder, J. Vay, E. Esarey, S. S. Bulanov, C. Benedetti, L. Yu, M. Chen, C. G. R. Geddes, and W. P. Leemans, Phys. Rev. Spec. Top. - Accel. Beams **17**, 101301 (2014).

[41] B. B. Pollock, C. E. Clayton, J. E. Ralph, F. Albert, A. Davidson, L. Divol, C. Filip, S. H. Glenzer, K. Herpoldt, W. Lu, K. A. Marsh, J. Meinecke, W. B. Mori, A. Pak, T. C. Rensink, J. S. Ross, J. Shaw, G. R. Tynan, C. Joshi, and D. H. Froula, Phys. Rev. Lett. **107**, 045001 (2011).

[42] T. P. Rowlands-Rees, C. Kamperidis, S. Kneip, A. J. Gonsalves, S. P. D. Mangles, J. G. Gallacher, E. Brunetti, T. Ibbotson, C. D. Murphy, P. S. Foster, M. J. V. Streeter, F. Budde, P. A. Norreys, D. A. Jaroszynski, K. Krushelnick, Z. Najmudin, and S. M. Hooker, Phys. Rev. Lett. **100**, 105005 (2008).

[43] N. H. Matlis, A. J. Gonsalves, S. Steinke, J. V. Tilborg, B. Shaw, D. E. Mittelberger, C. G. R. Geddes, and W. P. Leemans, J. Appl. Phys. **119**, 074501 (2016).

[44] S. Steinke, J. van Tilborg, C. Benedetti, C. G. R. Geddes, J. Daniels, K. K. Swanson, A. J. Gonsalves, K. Nakamura, B. H. Shaw, C. B. Schroeder, E. Esarey, and W. P. Leemans, Phys. Plasmas **23**, 056705 (2016).